Available online at www.sciencedirect.com
ScienceDirect
Geochimica et Cosmochimica Acta 70 (2006) 4933–4949
Geochimica
www.elsevier.com/locate/gca

Two-dimensional pH distributions and dynamics in bioturbated marine sediments

Qingzhi Zhu, Robert C. Aller *, Yanzhen Fan

Marine Sciences Research Center, SUNY at Stony Brook, Stony Brook, NY 11794-5000, USA

Received 16 March 2006; accepted in revised form 20 July 2006

Abstract

The seafloor is the site of intense biogeochemical and mineral dissolution–precipitation reactions which generate strong gradients in pH near the sediment-overlying water interface. These gradients are usually measured in one-dimension vertically with depth. Two-dimensional pH distributions in marine sediments were examined at high resolution (65×65 μm pixel) and analytical precision over areas of ~150 to 225 cm^2 using a newly developed pH planar fluorosensor. Dramatic three-dimensional gradients, complex heterogeneity, and dynamic changes of pH occur in the surficial zone of deposits inhabited by macrofauna. pH can vary by ±2 units horizontally as well as vertically over millimeter scales. pH minima zones often form in association with redoxclines within a few millimeters of inner burrow walls, and become more pronounced with time if burrows remain stable and irrigated for extended periods. Microenvironmental pH minima also form locally around decaying biomass and relict burrow tracks, and dissipate with time (~5 d). H^+ concentrations and fluxes in sandy mud show complex acid–base reaction distributions with net H^+ fluxes around burrows up to ~12 nmol cm^{-2} d^{-1} and maximum net reaction rates varying between −90 (consumption) to 120 (production) μM d^{-1} (~90 nmol cm^{-1} d^{-1} burrow length). Acid producing zones that surround irrigated burrows are largely balanced by acid titration zones along inner burrow walls and outer radial boundaries. The geometry and scaling of pH microenvironments are functions of diagenetic reaction rates and three-dimensional transport patterns determined by sediment properties, such as diffusive tortuosity, and by benthic community characteristics such as the abundance, mobility, and size of infauna. Previously, undocumented biogeochemical phenomena such as low pH regions associated with in-filled relict biogenic structures and burrowing tracks are readily demonstrated by two-dimensional and time-dependent images of pH and sedimentary structure.

1. Introduction

Intense biogeochemical and mineral dissolution–precipitation reactions in sedimentary deposits generate strong gradients in pH near the sediment-overlying water interface (Boudreau and Canfield, 1993; Reimers et al., 1996; Van Cappellan and Wang, 1996). Sediment pH changes are often dramatic, with ranges of ±1 to 2 units over millimeter to centimeter scales, and can be time-dependent (Cai et al., 1995; Marinelli and Boudreau, 1996). These distributions reflect not only the acid–base balances determined by early diagenetic reactions but also transport processes such as solute diffusion or advection which govern exchange between sediment and overlying water. Measurements of pH have traditionally been made using H^+ ion selective glass electrodes or fiber optical sensors, and have been restricted to individual points or vertical profiles (e.g., Cai et al., 1995; Hales and Emerson, 1997; Komada et al., 1998). Until very recently there have been no analytical techniques capable of quickly and accurately resolving the heterogeneous patterns of pH which can occur in deposits. Advances in digital imaging technology, however, have now permitted the extension of fiber-optic fluorosensor techniques to two dimensions and the development of so-called planar optodes. These planar sensors utilize the fluorescence imaging of sensing films containing solute specific fluorophores in contact with an environmental surface (e.g., Glud et al., 1996; Holst and Grunwald, 2001; Hulth et al., 2002). Planar imaging optodes have been used in

* Corresponding author.
E-mail address: raller@notes.cc.sunysb.edu (R.C. Aller).

0016-7037/$ - see front matter © 2006 Elsevier Inc. All rights reserved.
doi:10.1016/j.gca.2006.07.033

the measurement of O_2 distributions in sediments (Glud et al., 1996, 2001; Precht et al., 2004; Wenzhöfer and Glud, 2004), and sensors for NH_4^+, pH, and pCO_2 have also been developed for practical environmental applications (Strömberg and Hulth, 2001; Hulth et al., 2002; Zhu et al., 2005, 2006; Stahl et al., 2006).

In the present study, we utilize a rugged pH planar fluorosensor based on HPTS (8-hydroxy-1,3,6-pyrenetrisulfonic acid trisodium salt) which we recently developed, to resolve and quantify two-dimensional pH patterns and temporal dynamics in shallow water marine sediments. In addition to revealing continuous spatial distributions at high resolution, a major advantage of fluorosensor imaging is that compositional patterns can be directly related to visually evident physical structure, providing a basis for interpretation and generalization of any associated reaction processes. An additional advantage is that the instrumentation and software required for practical application are relatively simple and inexpensive. We demonstrate that pH can be highly heterogeneous and time-dependent in bioturbated deposits, with variations reaching ~2 pH units around irrigated biogenic structures. These examples show directly that use of mean pH values in the evaluation of mineral saturation states, adsorption equilibria, solute speciation, or quantitative diagenetic models can be a misleading indicator of reaction conditions in bioturbated deposits.

2. Methods

2.1. pH planar fluorosensor foil

The design, preparation, and analytical performance of the pH planar fluorosensor foil have been described elsewhere (Zhu et al., 2005). The pH sensitive fluorescent dye (HPTS) is covalently immobilized on the surface of a polyvinyl alcohol (PVA) membrane (~10 μm thick). The PVA membrane is underlain and supported by a clear polyester sheet (~110 μm). The pH sensor foil may be stored in a refrigerator up to 3 years or at room temperature for at least one year by sealing in an opaque bag. The foil is transparent and rigid, and shows bright green fluorescence at 540 nm with excitation bands located at 428 and 506 nm for the acid and base form of HPTS, respectively. The ratio of emission intensities at 540 nm following successive excitation at 428 and 506 nm is directly proportional to pH in contacting solutions over the pH range 5.5–8.6. The use of emission ratios, or ratiometric measurements, rather than a single steady intensity largely eliminates interferences from indicator photobleaching or foil heterogeneities, fluctuations of excitation light intensity, and minimizes effects of background fluorescence for practical environmental applications.

2.2. Sensor calibration

The operating principle of pH optical sensors is different from that of potentiometric methods. Potentiometric pH measurements depend linearly on the activity of hydrogen ions and a stable reference electrode, whereas optical measurements are a function of the concentration of the acid and base forms of the indicator, not of the activity of the hydrogen ions (King and Kester, 1989; Leiner and Hartmann, 1993). The dissociation of weak organic acid HPTS can be expressed as

$$\mathrm{HPTS} \leftrightarrows \mathrm{H^+} + \mathrm{PTS^-}$$

$$\frac{[\mathrm{HPTS}]}{[\mathrm{PTS^-}]} = \frac{[\mathrm{H^+}]}{K_a} \cdot \frac{\gamma_{\mathrm{H^+}}\gamma_{\mathrm{PTS^-}}}{\gamma_{\mathrm{HPTS}}} \quad (1)$$

where [HPTS] and [PTS^-] are the total concentrations of the acid form (HPTS) and base form (PTS^-) of HPTS in the optode. [H^+] is the total concentration of hydrogen ions.γ_{H^+}, γ_{HPTS} and γ_{PTS^-} are the total activity coefficients of hydrogen ions, HPTS, and PTS^- respectively. K_a is the thermodynamic dissociation constant for the reaction at the system fixed temperature and pressure.

For the fluorescence ratiometric method, the pH, defined as $= -\log[H^+]$ on the total H^+ concentration scale, is related to the ratio, σ, of fluorescence emission intensity of PTS^- to that of HPTS (Hulth et al., 2002; Kermis et al., 2002):

$$\mathrm{pH} = \mathrm{p}K'_a - \log\frac{(\sigma_{max} - \sigma)}{(\sigma - \sigma_{min})} - \log\frac{(\varepsilon_{PTS^-}\Phi_{PTS^-})_{\lambda_2}}{(\varepsilon_{HPTS}\Phi_{HPTS})_{\lambda_2}} \quad (2)$$

where σ_{min} and σ_{max} are the ratios at the most acidic and basic ends of the working range where total HPTS is dominated by HPTS and PTS^-, respectively. ε_{PTS^-}, Φ_{PTS^-} are the extinction coefficient and quantum yield of PTS^- at the base form excitation maximum λ_2, and ε_{HPTS}, Φ_{HPTS} are the extinction coefficient and quantum yield of HPTS at λ_2. The dissociation constant K'_a, is defined for the specific solution reference medium, in this case sea water at a fixed salinity ($\gamma \to 1$), consistent with use of the total [H^+] concentration scale and the dominance of activity coefficients by the major electrolytes in sea water (Hansson, 1973; Dickson, 1993). Concentrations in the present study are relative to total solution volume.

The total [H^+] convention requires that the composition of pH buffer standards match that of the application environment. In the present study, standard tris and pyridine buffers (pH 6.770, 8.073, 8.573 at 25 °C) were prepared in artificial sea water of varying salinity (Hansson, 1973; Millero, 1986; Dickson, 1993). For initial standardization and examination of pH sensor responses to buffers of varying salinity, small sections of sensor foils were fixed at ~30° to incident radiation within a custom cuvette filled with buffer solution. Fluorescence excitation–emission scans were made using an Hitachi F-4500 fluorescence spectrometer. During imaging applications, pH foils were standardized in two ways. In one method, sections of pH sensor foils were mounted on the inside front-face of 1 cm^2 methylacrylate cuvettes containing a series of standard buffers. The cuvettes were placed in a line and imaged as a set under the same conditions as sample analysis. In a second,

more preferred method, buffers were sandwiched as a thin film between a sensing foil and a second polyester sheet, creating permanent sealed and flexible thin film standard sheets (~250 μm thick) (Aller and Zhu, 2005). These thin film standards were cut into strips and mounted directly on a portion of the imaged surface, allowing simultaneous standardization and evaluation of possible interferences from background variation and scatter.

2.3. Optical instrumentation

The two-dimensional fluorescence imaging system is described elsewhere (Zhu et al., 2005). The plate pH optode is excited by the light from two LEDs with respective irradiation maximum at 420 and 500 nm, or by the light from a 300-W Xe UV/vis arc lamp which is controlled by a computer to change excitation wavelengths between 428 and 506 nm. The luminescent light emitted from the sensor foil is then imaged by a digital camera (Canon EOS 10D or 60D, 2048×3072 pixels) which is controlled by Canon Remotecapture 2.7 software. A Canon lens (model EF-100 mm) is used and an emission filter (540 nm) is mounted between the lens and camera to eliminate interferences from background signals and scattered light. In order to avoid strong reflected light, the fluorescence images are taken perpendicular to the sample plane with excitation light at an angle of incidence below 30°. All image analyses are performed with Maxim DL image processing software version 2.0X (Diffraction Limited) and Image-Pro plus version 4.1 for Windows (Media Cybernetics). The method for calculation of image intensity ratio (506–428 nm at each pixel) is described by Zhu et al. (2005). Images can be obtained with a pixel size of 10×10 to 65×65 μm (2048×3072 pixels) applied over areas of 2×3 and 13.2×19.8 cm, respectively. In this work, images were obtained with a pixel size of 65×65 μm.

2.4. Sediment samples

Sediment cores were collected from intertidal mudflat sites in Flax Pond, a back barrier salt marsh on the northshore of Long Island (New York, USA) in October, 2003. The undisturbed samples were transferred to the laboratory and kept in the dark at room temperature with constant aeration of overlying water (salinity = 27–28). The overlying water and the upper ~12 cm of the sediments were used for measurements. Sources of sediment in this area are unconsolidated glacial till from upland areas and tidal deposition of resuspended marsh sediment. The sediments are about 41–61% slit (dry weight), 25–44% sand, and 11–24% clay. Bulk organic carbon in Flax Pond sediments shows no clear seasonal trend and lies in the range of 2.12–3.12% (Montlucon and Lee, 2001). The concentrations of porewater ΣH_2S, Fe^{2+}, and Mn^{2+} are typically around 2–8 mM, ~100 and ~10 μM, respectively (M = moles · liter^{-1}), and O_2 typically penetrates 2–3 mm from oxygenated surfaces (Swider and Mackin, 1989).

Sediment box cores were also obtained from subtidal central Long Island Sound (USA) at a depth of 35 m in September 2003 (bottom water salinity = 27–28) using a Soutar style boxcorer. Macrofaunal population abundances at the site were depleted at the time of sampling (September), and sediment structure was close to being vertically stratified. Rectangular subcores of larger box cores were incubated as microcosms in the laboratory at 22 °C. The Long Island Sound sediment consists of >75% silt–clay. The surface few millimeters of the sediments are yellow-brown and are underlain by a zone of mottled yellow-black-grey sediment several decimeters thick. The concentration of organic carbon, pore water ΣH_2S, Fe^{2+}, and Mn^{2+} are typically ~2%, ~0, ~30 and ~100–300 μM, respectively, and O_2 penetrates 2–4 mm from oxygenated surfaces (Aller, 1980, 1994).

Homogenized mud samples were prepared by using surface sediment (0–2 cm) from a 15 m site in central Long Island Sound (September 2004). Sediment was gently mixed and sieved (1 mm), and then transferred into rectangular microcosm tanks for incubation with aerated, overlying water.

2.5. Spatial and temporal two-dimensional pH measurements

Glass walled microcosms, $20 \times 15 \times 6$ cm ($L \times W \times H$), initially open at the top and bottom (15×20 cm surfaces), were used for subcoring intact sediment within larger boxcores and for subsequent imaging. The larger inside faces of a glass microcosm were first covered with 14×20 cm pH optode films, and then the box was gently inserted into the sediment. After sealing the bottom, the sediment microcosm was filled with seawater, continuously aerated, and kept in the dark at room temperature (~22 °C). Glass walled microcosms were used for sampling of naturally intact sediments from both Flax Pond and central Long Island Sound. Microcosms were also used for incubation of initially homogenized sediment with or without added infauna.

In order to observe pH distribution changes as a function of time during infaunal burrow formation, several *Nereis succinea* (the common rag worm present at the sample site) were added into the microcosm cores obtained from Flax Pond. After an initial 1 day period of acclimation, pH fluorescence and visible images were taken daily for several weeks. During imaging, a black plastic film was vertically inserted in the overlying water at the rear of the microcosm to provide a uniform background.

The sides of intact sediment cores from central Long Island Sound were imaged for pH as done for sediment from Flax Pond. In addition, microcosms were partially filled with initially homogenized surface sediment from Long Island Sound, bottom water was added, and the sediment was allowed to exchange with the aerated overlying water for 3 weeks. The inside faces of the microcosm tanks were covered with a transparency film which was used as a placeholder until pH imaging. Sensor foils were

subsequently inserted between the placeholder sheet and the microcosm wall, and the placeholder sheet was gently withdrawn. One tank, 6 cm in thickness, was maintained without macrofauana in the dark at room temperature (22 °C) for 3 weeks to allow it to develop vertical pH gradients before measurement. A second microcosm tank had a thickness of 0.5 cm but otherwise contained a portion of the same sediment. The inside front-face of the tank was covered with a 14×16 cm fluorosensor foil. This thin microcosm was incubated with overlying water in the dark at room temperature (22 °C) for one week in the presence of one *Nepthys incisa*, a polychaete worm common in muds of central Long Island Sound.

For comparison of optical and potentiometric measurements, pH profiles in the intact sediment microcosms from Long Island Sound and in the originally homogenized sediment were measured using a Thermo Orion pH meter (Model 290A) equipped with a VWR SympHany mini-electrode (tip diameter 0.5 cm, Ag/AgCl reference) at 1-cm depths interval by direct insertion of the electrode during core extrusion.

The pH of overlying seawater in the samples did not exceed 8.2. The sensor optode was calibrated in the pH range of 6.2–8.2, and the corresponding pH scale between 6.2 and 8.2 was used for the 2-D pH distributions.

2.6. Proton flux and reaction calculations

Estimates of two-dimensional [H^+] flux and net reaction patterns were made within image planes using measured concentration differences between pixels. No corrections for solute reflection or possible geometrical distortions on the image plane were made. In order to minimize amplification of local differences between pixels during model calculations, the original pH images were first converted to equivalent total [H^+], (=C), concentration images, and Gaussian filtered over 7×7 pixel neighborhoods. Individual pixel columns and rows were then Gaussian smoothed in succession vertically and horizontally to eliminate minor remaining irregularities interpreted as residual local noise. Smoothed concentration patterns in randomly selected columns and rows of single pixel width were visually compared, using graphical overlays, directly with unfiltered distributions to insure no loss of significant concentration pattern information and to double check the programmed procedure. Vertical ($C_z = \partial C/\partial z$) and horizontal ($C_y = \partial C/\partial y$) concentration gradients between pixels within the smoothed concentration image were calculated using a standard five point central difference scheme (4th order error). The vertical and horizontal diffusive fluxes, J_z and J_y, were estimated from concentration gradients assuming:

$$J_z = -\varphi D_s C_z \tag{3a}$$

$$J_y = -\varphi D_s C_y \tag{3b}$$

where φ is the porosity, D_o is the free solution diffusion coefficient of H^+ in sea water, and the whole sediment diffusion coefficient $D_s \sim \varphi^2 D_o$. Porosity and diffusion coefficients were assumed isotropic and constant, with $\varphi = 0.8$ (based on average water content) and $D_o = 7.56\ \text{cm}^2\ d^{-1}$ ($T = 22$ °C; salinity = 25; Boudreau, 1997). The semi-permeable properties of burrow linings and mucus secretions were assumed to be of minor influence in this context (Hannides et al., 2005), and possible nondiffusive transport by meiofauna was ignored (Aller and Aller, 1992; Glud and Fenchel, 1999). In addition, because detailed solution and particle surface compositions are unknown, interdiffusion, exchange, and cross-coupling between charged species were not taken into account but likely lower the diffusion coefficient of H^+ (Farr et al., 1970; Boudreau et al., 2004). Model estimates are therefore maxima in that regard. The flux vector magnitude, $|\vec{J}|$, within the image plane at each pixel was calculated as:

$$|\vec{J}| = \sqrt{J_z^2 + J_y^2} \tag{4}$$

Assuming local steady state concentration distributions, net reaction rates, R, were estimated using the two-dimensional Laplacian of the smoothed concentration distribution and a standard five point central difference scheme (4th order error):

$$R = -D_s \nabla^2 C = -D_s (C_{zz} + C_{yy}) \tag{5}$$

3. Results

3.1. Sensor performance

The general performance and practical characteristics of the planar pH fluorosensor have been discussed elsewhere in detail (Zhu et al., 2005). The HPTS optode foils show a single emission band at 540 nm and dual excitation bands at 428 and 506 nm. As pH increases, for example, the emission following excitation at 428 nm (acid form) decreases while emission from excitation at 506 nm (base form) increases. An isosbestic point is present at 444 nm. The ratio of the maximum emissions following 506 and 428 nm excitation correlates well with pH change in the range of 5.8–8.6 (Fig. 1A).

Optode response is insensitive to dissolved oxygen and temperature. It is, however, sensitive to the ionic strength of the contacting solution (Wolfbeis and Offenbacher, 1986; Hulth et al., 2002; Kermis et al., 2002). The dependences of fluorescence emission ratios on total [H^+] at different sea water salinities at $T = 22$ °C are shown in Fig. 1B. The $pK'_a = 7.06$ at $S = 35$, and increases with decreasing salinity. The pK'_a on the NIST (H^+) activity scale is 7.24 (dilute Tris–HCl buffers). There is only a minor effect of salinity change on relative sensor response in the salinity (S) range $25 < S < 35$. Specific dissolved metal ions and anions, for example Ca^{2+} (200 mM), Mg^{2+} (200 mM), Mn^{2+} (10 mM), Fe^{3+} and Fe^{2+} (1 mM), SO_4^{2-} (20 mM), PO_4^{3-} (100 mM), NO_3^- (20 mM), and S^{2-} (1 mM), do not interfere with the

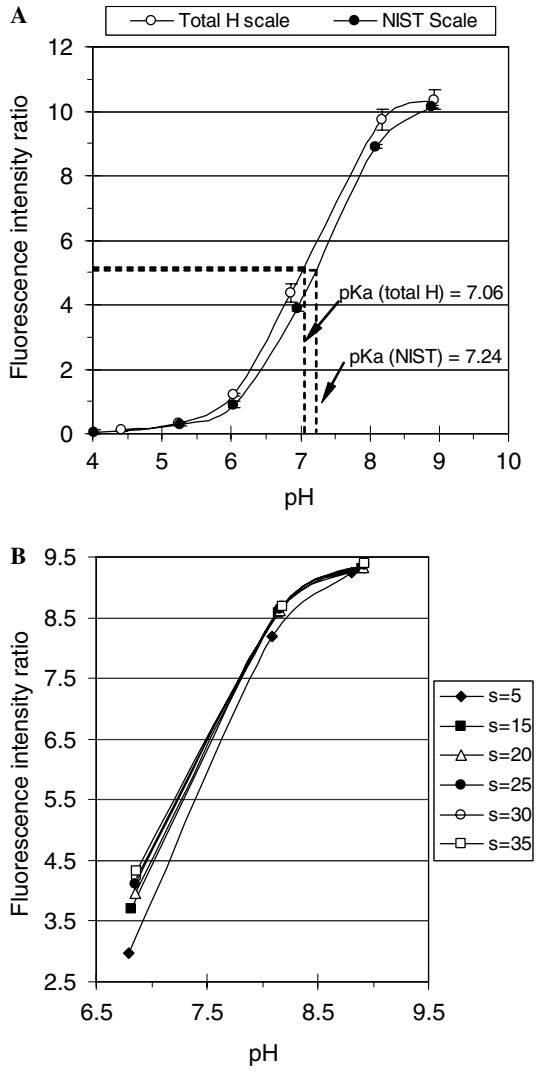

Fig. 1. (A) Comparison of fluorescence response and pK_a of the pH sensor in NIST scale buffers (0.1 M Tris–HCl buffer) and pK'_a in total [H] scale synthetic seawater buffers ($S = 35$, 0.01 M Tris–HCl). (B) Effect of salinity (S) of synthetic seawater buffers on pH sensor response.

pH measurement in Tris–HCl buffer with salinity 31 (higher concentrations of the ions above that indicated in parentheses were not tested).

The precision of response between different sensor foils over the pH range of 5.8–8.6 is <5.5% relative standard deviation (RSD) (3 optode films, 3 trials each). The pH measurement precision between pixels across the same sensor film at a single pH in sea water is 0.02 pH units using the digital camera. The fluorosensor response time is ~1 min for a 90% signal response after a stepwise change from pH 6–8, and 2 min for equilibrium. Full reversibility across a single instantaneous 2 units pH change can require up to 5 min for complete equilibrium. The sensor foil responses are stable for at least hundreds of cycles through the full pH range (Zhu et al., 2005). Optode foils can also be kept in marine sediment with overlying seawater for at least 3 weeks at 22 °C without performance change.

3.2. pH distributions in vertically stratified sediment and analytical verification

A two-dimensional pH distribution within an intact sediment core obtained from subtidal central Long Island Sound at 35 m depth is shown in Fig. 2. The sediment core was collected and imaged in September 2003. Macrofaunal population abundances were depleted at the time of sampling, and the sediment physical features were close to being vertically stratified. The corresponding two-dimensional pH distribution pattern in Fig. 2A shows the vertically stratified pH pattern in this sediment. The image (13.2×17 cm) is composed of 2048×2635 pixels with resolution of $\sim 65 \times 65$ μm. The pH distribution is largely homogeneous in the overlying water and averages ~8.0. pH drops dramatically at the water-sediment interface. A pH boundary layer is clearly visible at the water-sediment interface, reflecting the balance between the proton flux from sediment to overlying water and stirring of the water during aeration. A pH minimum zone within the sediment at a depth of 1–3 cm is also visible, with an average pH ~6.6. Below the minimum, the pH gradually increases and becomes almost homogeneous. Although the pH distribution symmetry is vertically stratified overall, there is significant lateral variation in zonal thickness. The averaged pH vertical profile of Fig. 2A calculated from each horizontal pixel layer of the image was compared with that obtained by a glass pH mini-electrode inserted over 1-cm intervals. Comparison of the two techniques shows good agreement between the averaged pH values. Slight differences between the two pH profiles can be explained by lateral variation of pH in the deposit. The pH profiles obtained by the plate sensor and by the electrode were not at exactly the same positions nor do they integrate the same volumes. The higher standard deviations within the pH minimum zone apparently reflect the lateral variation in zonal thickness.

In order to further confirm the measurement accuracy and performance of the fluorosensor, the pH distributions in originally homogenized sediment from central Long Island Sound were also measured and compared using both the fluorosensor and electrode. A pH sensor foil was carefully inserted into the tank along its inner front surface. Because the pH distribution pattern may have been slightly disturbed when the sensor foil was introduced into the sediment, the foil was allowed to equilibrate for 1 h prior to final imaging (experiments show that a stable sediment image is reached within ~15 min. after foil insertion). After imaging, sediment was profiled using the glass mini-electrode inserted over 1-cm vertical intervals at six locations. The laterally averaged pH vertical profiles calculated from horizontal pixel layers in the pH image and grouped vertical profiles obtained using the pH mini-electrode again show that the mean values predicted by the two methods are analytically indistinguishible (Fig. 2C). For both methods, pH distributions are homogeneous in the

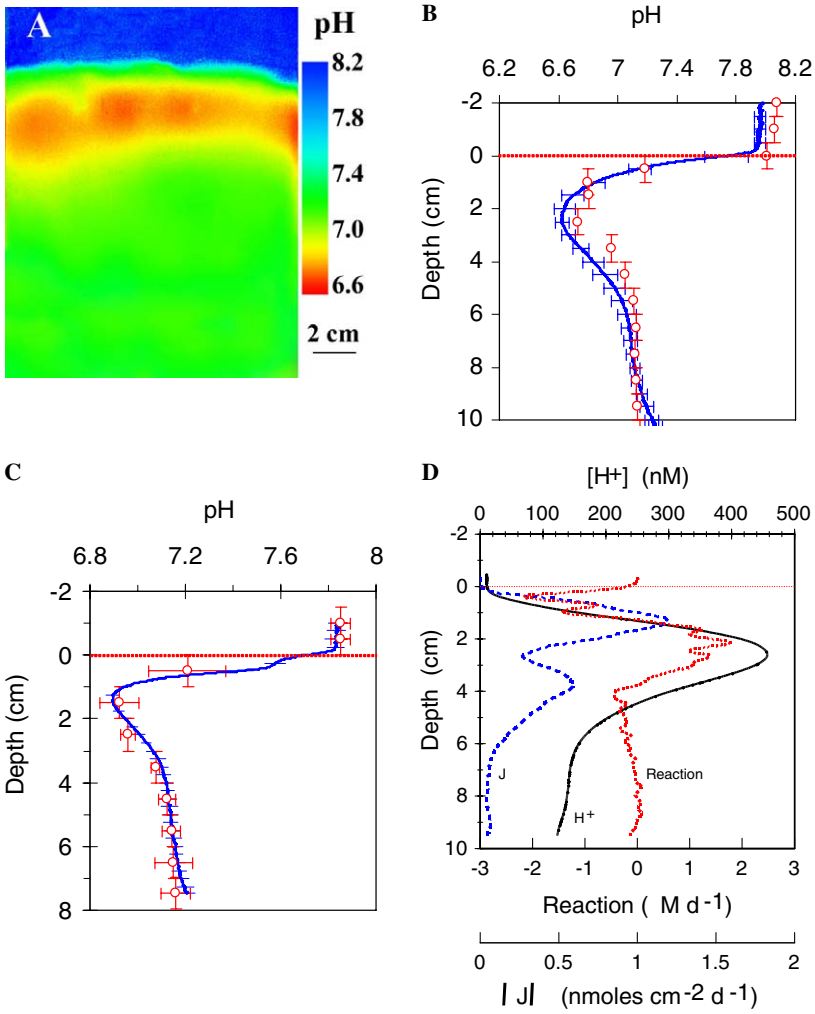

Fig. 2. pH distribution pattern in a largely vertically stratified sediment. (A) Two-dimensional pH distribution pattern (pseudocolored) in subtidal core and overlying water obtained from central Long Island Sound (35 m depth) (September 2003). No distinct burrows are present. (B) The average vertical pH profile of (A) calculated from each horizontal pixel layer (continuous line, ±SD) and that obtained from a minielectrode (open dots) at 1-cm interval measurements. (C) pH distributions in originally homogenized surface sediment obtained from central Long Island Sound (September 2004) measured with the planar fluorosensor (line) and a glass pH mini-electrode (dot) over 1 cm intervals ($n = 6$). The standard deviation of the fluorosensor measurements were calculated from each horizontal pixel layer (bar). (D) Total H^+ concentration distributions, flux vector magnitudes, and net reaction rate averaged across the center 5.75 cm in (A). Model estimates using Eqs. (3)–(5) were made in the image plane only.

overlying water and average ~7.85. Below the water-sediment interface, the pH drops sharply and in this case forms a pH minimum zone around 1 cm depth. A thin diffusive boundary layer is evident (Fig. 2B and C). In contrast to the naturally structured sediment, horizontal pH distribution in the homogenized sediment is almost constant with only a small standard deviation within each horizontal pixel layer (0.02–0.04 pH unit variation). The small standard deviation confirms the inherent precision of the fluorosensor measurements. The imaged pH standard deviation in overlying water ~0.04 was higher than that in sediment ~0.03 because sediment particles in the overlying water became attached to the sensor foil during water aeration and created local interferences. When the foil was utilized to measure the pH in clear seawater, a homogeneous two-dimensional pH image was obtained with standard deviation of ~0.02; superior to the precision of the pH electrode in overlying seawater of ~0.04. The standard deviations from mini-electrode measurement in sediment ranged from 0.04 to 0.16 pH units.

Model calculations of the 2-D flux magnitude and net reaction rate distributions Eqs. (3)–(5), were horizontally averaged across the image plane (strips 5.75 cm extent), and show the relative patterns with depth (Fig. 2D). Averaging across the image plane obscures local variability of the parameters, for example, the maximum flux magnitudes and reaction rates in the broad acidification zone between 1 and 3 cm can exceed 1.5 nmol cm^{-2} d^{-1} and 6 μM d^{-1}, respectively, although averages are 1.2 cm^{-2} d^{-1} and 2 μM d^{-1}, respectively (Fig. 2D).

3.3. pH distributions and dynamics in burrowed sediments

3.3.1. General patterns

When distinct irrigated burrow structures are present, pH distributions are spatially complex and highly time-de-

pendent (Figs. 3, 4). In one experimental time series with a natural sediment microcosm, multiple burrows of *N. succinea* (common rag worm in sampling site) were followed over a 16 day period. The patterns at 8 days illustrate the biogenic spatial heterogeneity and pH variation generated within specific depth horizons. A horizontal transect at 1 cm shows relatively regular oscillation of ~2 pH units with a characteristic spatial repeat scale of ~3 cm associated with the spacing of irrigated burrow structures (Fig. 3). These spatial patterns are time-dependent (Fig. 4) and the particular geometric scalings are dependent on animal size, abundance, and burrowing activity patterns. The horizontally averaged vertical profile demonstrates in this case that at any given depth within the upper 6 cm, a total range around the mean pH of ~2 units is found, with a standard deviation of ±0.5. The variation damps sharply below the burrowed zone at 6 cm.

In most cases, burrowing patterns are not static in the bioturbated zone. The corresponding three-dimensional pH distributions are also not static, and change as infauna move and rework sediment. Two time series taken from separate Flax Pond sediment microcosms demonstrate the types of local and bulk pH dynamics that can occur. In one example, five *N. succinea* formed multiple burrows of varied stability over a 16 day period, a number of which intersected the imaging plane (Figs. 3 and 4). A *Nereis* burrow (righthand side, Figs. 3 and 4) was constructed on the first day and intermittently utilized thereafter. Even though the burrow was intermittently inhabited, its main structure remained stable during the experiment period. The corresponding pH images show that a stable distribution is maintained around this burrow, with an intense pH minimum zone within the burrow wall surrounding the burrow center. In the middle of the tank, however, several burrows were constructed and abandoned in succession. The pH distributions followed comparable dynamics to the changes in physical structure and animal activity. Initially formed *Nereis* burrows were localized sites of high pH associated within the irrigated burrow centers. Transient, lower pH regions began to form almost immediately within sediment around parts of the irrigated burrow centers, but these zones dissipated if burrows were abandoned. The $[H^+]$ concentrations in the center abandoned *Nereis* burrows increased to the range in the surrounding pore water within about two days (10 vs. 12 days, Fig. 4). This phenomenon demonstrates that stagnant voids created by *Nereis* began

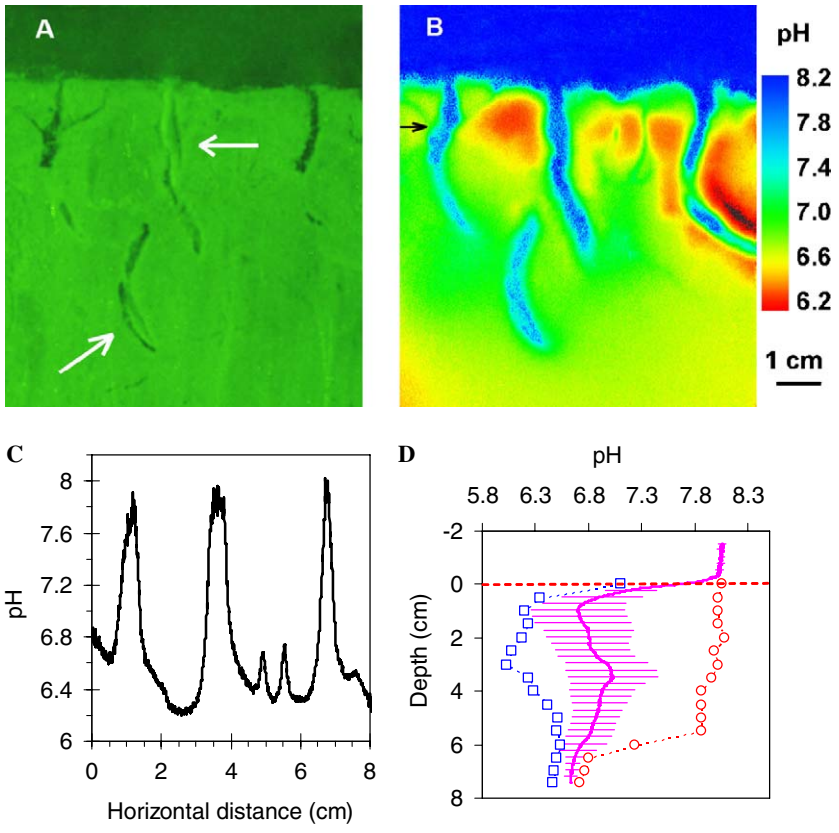

Fig. 3. pH distribution pattern in bioturbated marine sediment. (A) A visible image (green band) of intertidal sediment from Flax Pond (Long Island, USA) (October 2003) incubated for 8 days in the presence of *N. succinea* (white arrows). At least four burrows formed by the animals are evident at the time of imaging. The two burrows in the middle of the image are inhabited; the rightmost burrow structure was formed on day 1, and remained stable and intermittantly utilized thereafter; the leftmost burrow is younger and was formed on day 8. (B) Corresponding two-dimensional pH distribution of sediment (A). (C) The horizontal pH profile extracted along the black arrow in panel B. (D) The average vertical pH profile of panel B (horizontal average, ±SD) with minimum (square) and maximum pH (circle) in the calculated layer.

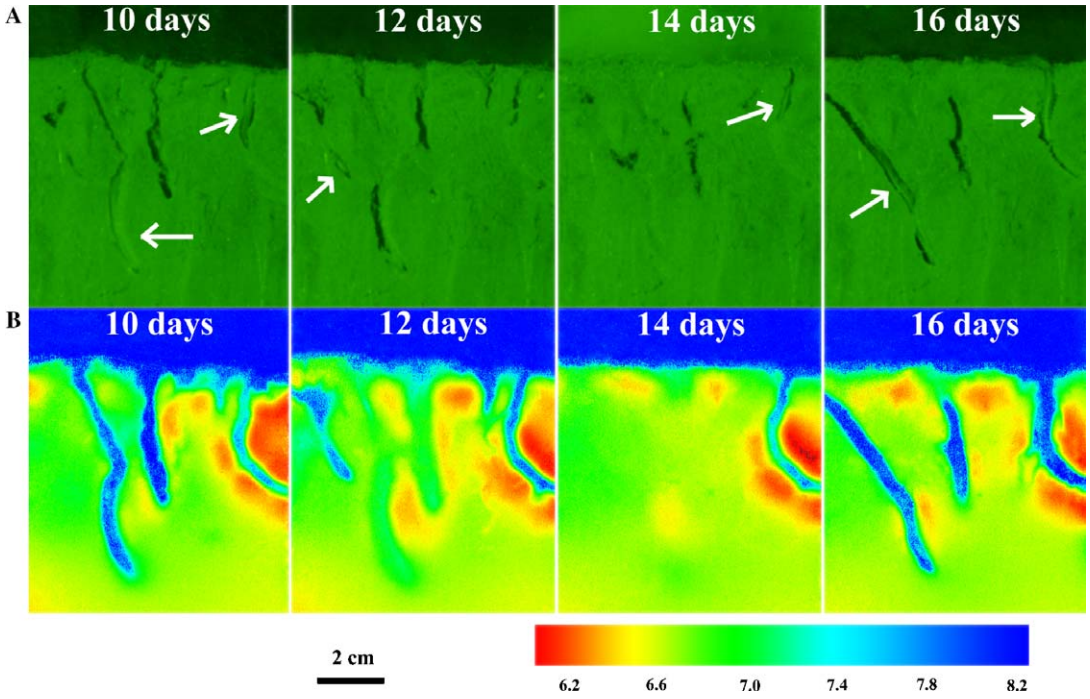

Fig. 4. Time series of visible images (row A) of intact Flax Pond sediment (October 2003) reworked by several *N. succinea* and the corresponding dynamic two-dimensional pH distributions (row B) subsequent to Fig. 3 (8 days). The rightmost burrow structure was formed on day 1, and remained stable and intermittantly utilized thereafter. The burrows in the middle of the image were modified episodically, and abandoned entirely from day 12 to 14. White arrows represent *N. succinea* in the burrows.

to re-equilibrate with surrounding sediment after ventilation ceased. Localized low pH zones formed around these abandoned but open structures, however, can persist for at least 2 days (Fig. 4). Burrows clearly act as a conduit for acid flux into the overlying water. For example, a low pH plume can be seen exiting the sediment from an irrigated burrow which lies out of the plane of the image in Fig. 5C, providing a direct evidence of sedimentary solute exchange with overlying water. Similar acidified plumes were observed by Stahl et al. (2006) and Zhu et al. (2006) using fluorescence lifetime pH and ratiometric pCO_2 imaging systems respectively.

3.3.2. Quantitative spatial and temporal concentration–reaction distributions

As shown in the time series, and most completely resolved in the second example (Fig. 5), if a *Nereis* burrow is formed and maintained for an extended period, a low pH radial halo tends to steadily grow in around it. The time-dependent, two-dimensional concentration, flux magnitude, and net reaction rate patterns around one burrow sector, which was inhabited for 14 days, demonstrate the progressive changes that can occur after burrow formation (Fig. 6). Concentration gradients were established immediately, and pH initially increased along the burrow wall as H^+ diffused into the alkaline irrigated burrow center. After a period of acclimation, in this case between 6 and 8 days, an obvious region of net acid production began to form rapidly within the sediment a few millimeters from the inner burrow wall, and acidification of the zone intensified progressively thereafter.

Calculations, using Eqs. (3)–(5), of the flux magnitude and net reaction rate distributions associated with the zonal ingrowth, show the relative patterns and the spatial variations that can occur along the burrow wall (Fig. 6). These calculations are approximate in that they utilize only concentration patterns measured within the image plane and because a maximum diffusion coefficient for H^+ is assumed. Because of uncertainty in the exact diffusion geometry and reaction rates within sediment away from the image plane, and because of the agreement between electrode and fluorescence based measurements (Fig. 2B and C), no corrections were made for solute reflection (no flux condition) perpendicular to the image. The exact effect of cutting the radial diffusion geometry around a burrow by the sensor plane depends on the relative position of the burrow–image plane intersection and the reactions governing pH (e.g., reactant supply, kinetics), and can be a function of time after insertion (based on finite element transport–reaction model calculations not shown). Assuming that pH contours are related directly or indirectly to O_2 sourced from burrow water, if the optode plane intersects a circular burrow wall such that the wall arc angle remaining within the sediment is 2π (optode plane tangent to burrow) or $>\pi$, the pH contours around the burrow should appear expanded on the image relative to the initial radial distribution (up to $\sim\sqrt{2}X$, Frederiksen and Glud, 2006). If the optode plane cuts through the center of a burrow (e.g. lies along a diameter, with residual arc angle π), the true radial patterns should be accurately imaged. As residual wall arc angle becomes $<\pi$, the apparent radial contours at steady

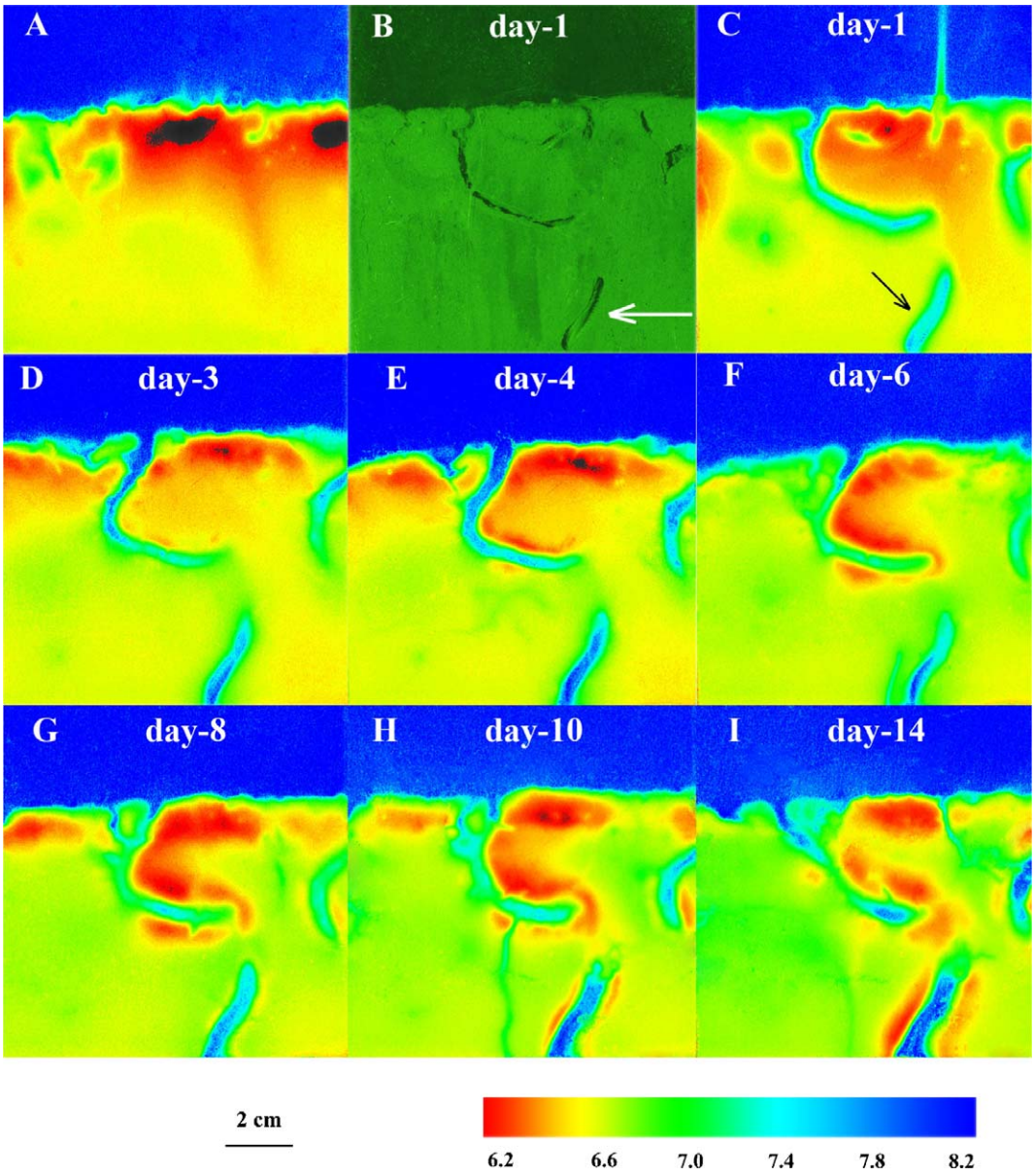

Fig. 5. Two-dimensional pH distributions and dynamic changes around burrows in an intact intertidal sediment core obtained from Flax Pond (October 2003), which was incubated for 14 days in the presence of *N. succinea* (white arrow). (A) Two-dimensional pH distribution in original sediment without burrows. (B) Visible image of sediment on the first day after adding five *N. succinea* (common rag worm in the sample site) into the sediment. The middle burrow was created on the first day and intermittently utilized thereafter. Although the animal slightly modified it, the burrow remained relatively stable for two weeks. The bottom section (white arrow) was continuously inhabited after formation and remained stable during the measurement period. (C–I) Two-dimensional pH distributions and dynamics around the burrows at different times (1–14 days).

state will contract. Images in the present study are assumed to intersect close to burrow diameters, and possible alteration of radial symmetry in the image is ignored.

A time series of radial profiles taken from the center of the irrigated burrow, across the burrow wall, and into surrounding sediment demonstrates the progressive formation and expansion of the acid production zone within the burrow wall (Figs. 6 and 7A). After 10–14 days, the $[H^+]$ concentration varied radially by more than 800 nM over a few millimeters. The concentration gradients along a radial coordinate, r, centered in the burrow water ($r = 0$ cm), show that the acid production zone (r range ~0.5–1 cm) is bounded by radial zones where acid is consumed along the inner burrow wall (r range ~0.24–0.5 cm) and within burrow water (0–0.24 cm), and also within surrounding sediment away from the burrow (r range ~1 to 1.8 cm). Thus, for a continuously inhabited *Nereis* burrow, there is a zonal reaction variation of net acid consumption, acid production, and acid consumption extending radially from the inner burrow wall into surrounding sediment. The maximum magnitude of the acid flux in this particular example reaches 12 nmol cm^{-2} d^{-1} with average directions in the image plane both towards and away from the burrow wall (Fig. 7B). The corresponding maximum net reaction rates

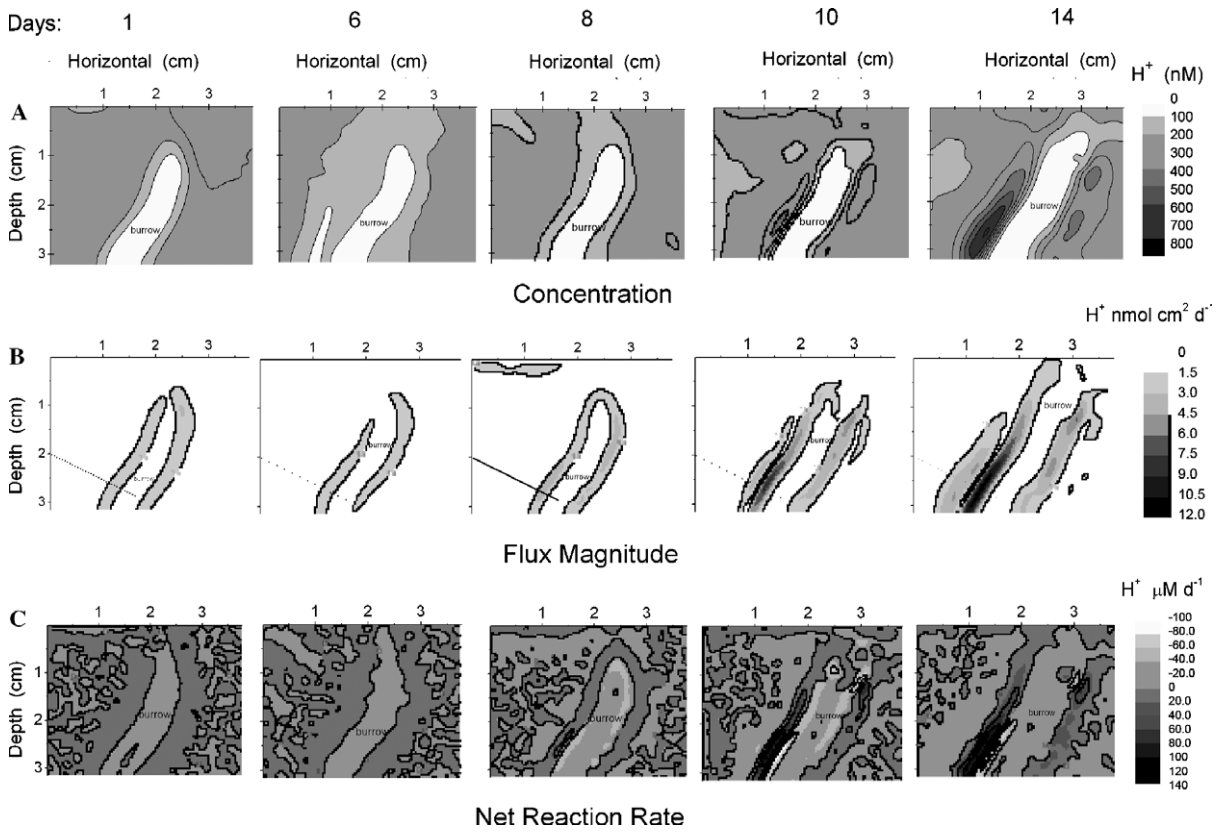

Fig. 6. (A) Time series contour maps of $[H^+]$ concentrations (nM) centered around the burrow bottom section indicated by the white arrow in visible image Fig. 5(B). (B) Time series flux magnitude contours (nmol cm^{-2} d^{-1}) corresponding to $[H^+]$ concentrations in (A). The dotted line corresponds to the position of the black arrow in Fig. 5(C), and marks the site of the radial profile patterns of Fig. 7. (C) Time series net reaction rate (μM d^{-1}) contour maps of $[H^+]$ corresponding to concentration patterns in (A). All calculations are made within the image plane only.

vary between ~120 μM $[H^+]$ d^{-1} production within the acid production zone and ~−90 μM $[H^+]$ d^{-1} within the inner acid consumption zones (Fig. 7C). These are about 20X higher than model rates observed during fall at the 35 m Long Island Sound site (Fig. 2D).

Assuming ideal radial symmetry of the reaction distributions around the burrow, the reaction rate functions obtained from the profiles can be numerically integrated to produce a hypothetical zonal average rate per burrow length (nmol cm^{-1} d^{-1}):

$$\bar{R} = 2\pi \int_{r_1}^{r_2} R(r) r \mathrm{d}r \tag{6}$$

The individual radial zone limits for integration were chosen as the burrow wall ($r_1 = 0.24$ cm for innermost zone) and the successive zeros of the reaction rate function (e.g., r_1, $r_2 = 0.44$, 0.70, 1.31 cm for day 8), giving inner ($\bar{R}_{\mathrm{I}}$), middle($\bar{R}_{\mathrm{II}}$), and outer($\bar{R}_{\mathrm{III}}$) reaction zones having radial annuli in the general range: 0.24–0.5, 0.5–1, and 1–1.8 cm (the specific integration limits within these zones are a function of time; Fig. 7C). In the present example, the exact choice of the burrow radius does not strongly influence the values of the innermost zone integral. The average $\bar{R}_{\mathrm{II}}$ in the acid production zone showed a rapid increase beginning between 6 and 8 days after the burrow was established (Fig. 7D). Although the net acid production rate continued to increase throughout the observation period, there is a hint of a slope change and a decrease in the rate of change of the reaction rate near day 14, implying a possible approach to steady state conditions. The time dependence of acid consumption within inner and outer zones mirrored the acid production rate. The inner burrow wall zone, $\bar{R}_{\mathrm{I}}$, had a consistently higher rate of integrated acid consumption than surrounding sediment but both zones had a similar overall importance (Fig. 7D). Although the acid consumption rate per volume pore water (R) is lower in the outer neutralization zone than in the inner (Fig. 7C), because of the increasing mass of sediment associated with radial symmetry, the spatially integrated outer zone has a comparable role to that of the innermost zone in terms of total acid titration. The integral across all three radial zones, $\sum \bar{R}$, (e.g., r range ~0.24 to 1.8 cm) demonstrates that a large proportion of the acid production was neutralized locally within the sediment near the burrow. However, the positive increase in $\sum \bar{R}$ with time indicates that the burrow produced a net flux of acid into overlying water (Fig. 7D).

The complex concentration and reaction patterns that can form around a single burrow structure, and the similarities of radial zonations near burrows compared to the vertical zonation near the sediment-overlying water interface are demonstrated by a 10-day-old *Nereis* burrow located

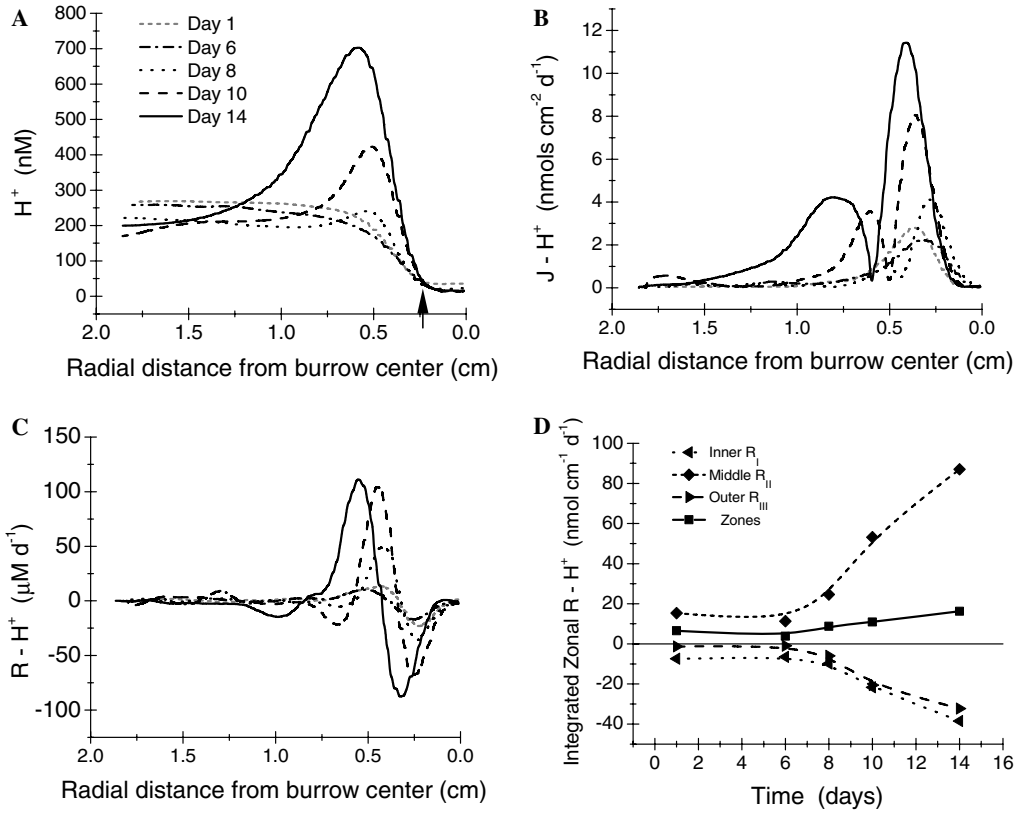

Fig. 7. (A) Time series radial profiles of $[H^+]$ concentrations (1–14 days) located along the black arrow in Fig. 5C and dotted lines in Fig. 6B showing ingrowth of acidification zone. The burrow water center is located at 0 cm and the arrow indicates burrow wall. (B) Time series radial profiles of the magnitude of the two-dimensional flux vector. The location of the zero net flux corresponds to the concentration maximum in (A) (approximately because of two-dimensional gradient). Fluxes to the right of the zero net flux are toward the burrow wall and fluxes to the left are away from the burrow. (C) Time series radial profiles of net [H+] net reaction rate showing ingrowth of acid production (+) and consumption (−) zones as a function of distance from the burrow center. (D) Integrated radial zone reaction rate per length of burrow within each primary reaction zone (I, II, and III), the individual boundaries of which are defined by the zeros of the reaction function in (C). The middle zone, $\bar{R}_{II}$, shows a rapid increase in acid production beginning between 6 and 8 days. The reaction rate integral across all radial zones ($\Sigma\bar{R}$) increases only moderately with time, showing that this acid production is largely balanced by titration in adjacent regions of the burrow wall and surrounding sediment.

in the center of Fig. 5 (Fig. 8). In this example, a dense network of small burrows was formed near one side of the larger structure (left side) and, because of their close packing, inhibited development of a distinct acidification zone in that region. The planar geometry at the sediment-overlying water interface resulted in relatively symmetrical bands of acid consumption rates, (R), above and below the main acid production zone. The rates on the underside (deeper) of the acid production zone tended to be high compared to that found in the outermost radial zone of acid titration around the *Nereis* burrow, although the roles of the zones were similar in that roughly $\frac{1}{3}$ to $\frac{1}{2}$ of the integrated acid production is titrated in each case due to the different geometrical weighting of the reaction regions (planar versus radial).

3.3.3. pH distributions around infilled burrows and infauna

Variations in pH can be associated with infilled, relict biogenic structures, as shown by experiments with *N. incisa* in initially homogenized sediment (Fig. 9). Like *Nereis*, the centers of burrows actively or intermittently irrigated by *Nephtys* were maintained at higher pH values than surrounding sediment. In contrast, a series of burrows successively formed and abandoned by *Nepthys* became sites of substantially lower pH than the ambient deposit after they either collapsed or were infilled (Fig. 9). The low pH regions associated with such burrow fill and relict biogenic structures dissipate after approximately one week (time series data not shown). The body surfaces of *N. incisa* were also found to differ distinctly from burrow water and ambient sediment pH, with typically lower values of ~6.8 (Fig. 9B). In contrast, the pH of body surfaces of *N. succinea* were usually indistinguishable from seawater (~8.0), demonstrating differences between infaunal species.

3.4. pH distributions and localized decay of reactive organic matter

The local pH distributions associated with the anaerobic decay of an entombed *Nereis* worm body in muddy sand at 10 cm depth were followed for a week period (Fig. 10).

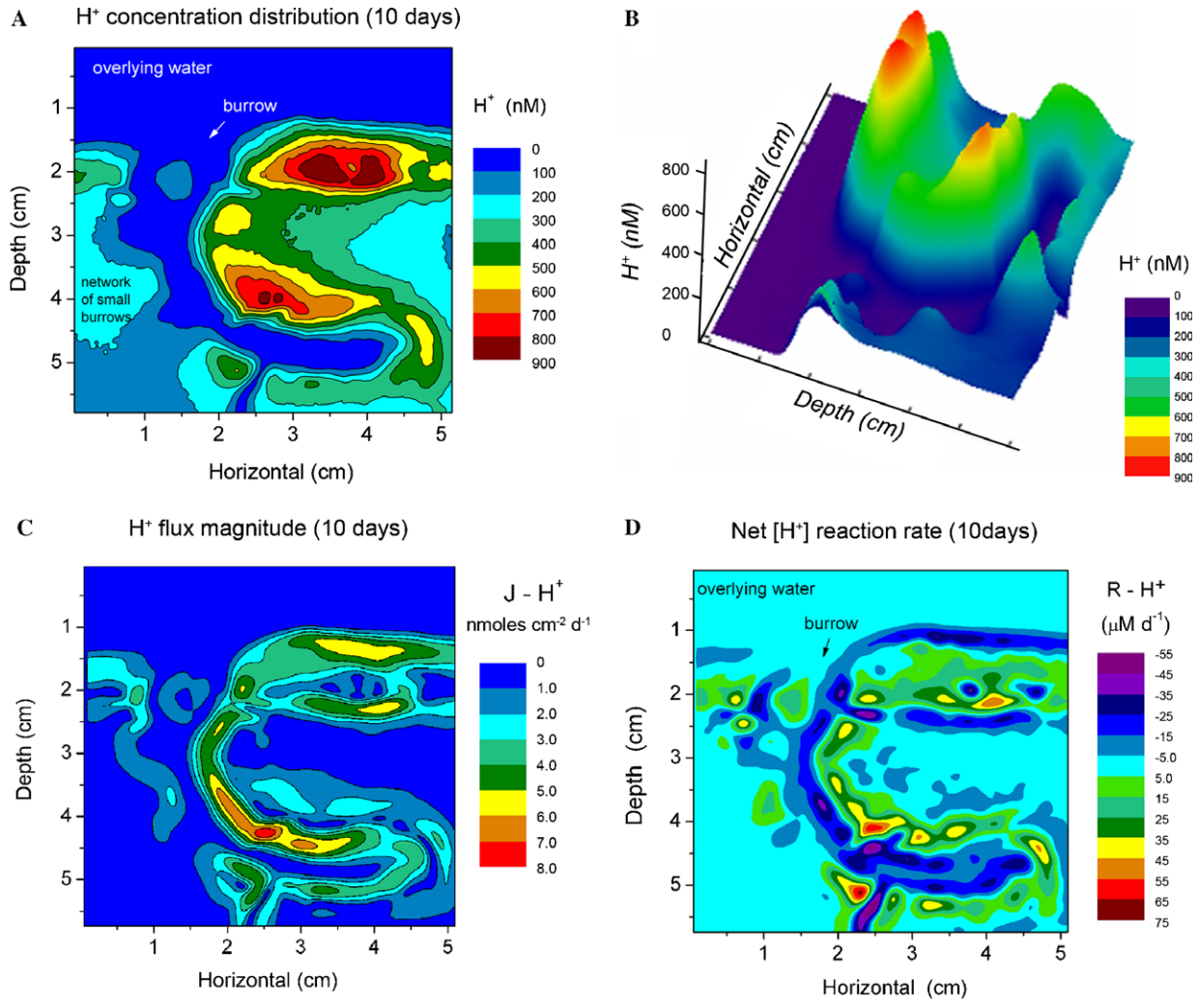

Fig. 8. (A) [H^+] concentration contour map of upper portion of the *Nereis* burrow centered in Fig. 5 at 10 days. On the righthand side, the concentration patterns associated with the redoxcline below the surfacemost sediment–water interface are comparable to those in the burrow wall. A dense network of small burrows became established on the lefthand side and prevented ingrowth of distinct acidification zones in that region. (B) Perspective view of [H^+] concentrations along sediment–water interface in (A). (C) Two-dimensional flux vector magnitude contours corresponding to the distributions of (A). (D) Net reaction rate contour distributions show that the radial geometry of reaction patterns around the burrow results in lower net reaction rates per volume pore water away from the burrow acidification zone compared to the consumption zone underlying the planar acidification zone near the sediment–water interface.

Visible images show that after 5 days, the body was completely decomposed and a cavity was formed at the original site. The time series pH distributions demonstrate that on the first day, a strongly acid region with pH $\leqslant$5.9 was centered on the decaying body. Acid diffused rapidly into the surrounding sediment, and by day 2, the pH at the center of the decaying mass began to increase slightly and the acid 'cloud' expanded. Actively irrigated burrow structures were formed nearby the decaying body but did not directly penetrate the low pH zone. By day 5, the pH distribution associated with the residual cavity was indistinguishable from ambient sediment. The corresponding pH profiles across the local decay zone are shown in Fig. 10(D), demonstrating the rapid dispersion and titration of metabolic acids. Part of the acid loss may be attributed to the presence of nearby irrigated burrows and diffusive transport into alkaline micro-environments.

4. Discussion

The geometric patterns and scaling of pH in the surface regions of sedimentary deposits can vary substantially depending on diagenetic transport–reaction conditions determined in large part by benthic fauna. When distinct biogenic structures such as burrows and tubes are absent, pH distributions are dominated by vertical zonation and have minimal horizontal variation. In such cases, simple vertical profiles can largely define pH patterns, although pH zones may expand and contract laterally due to changes in a range of biogenic and physical factors such as particle reworking activity and biogeochemical reactant availability (Fig. 2). When biogenic structures are present, however, sedimentary pH distributions are highly heterogeneous and time-dependent (Figs. 3 and 4). Complex, three-dimensional pH patterns are formed, the spatial scaling and

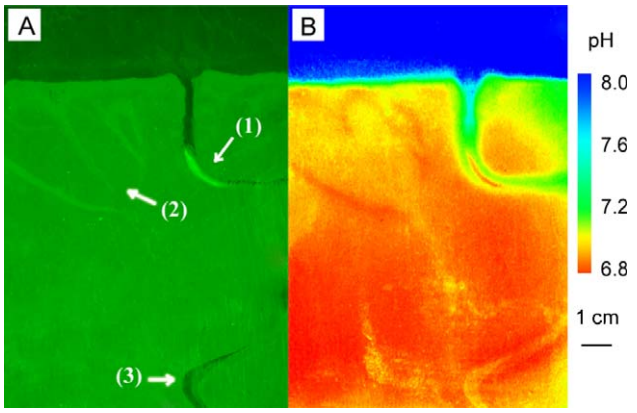

Fig. 9. (A) Side view of originally homogenized surficial sediment obtained from Long Island Sound (15 m depth; September 2004) and containing one *N. incisa* (polychaete worm). (1) indicates the inhabited burrow and worm, (2) represents completely infilled relict burrows and (3) is an abandoned burrow sector open to overlying water. (B) The corresponding pH distributions of panel (A) demonstrating low pH regions associated with relict infilled burrows.

dynamics of which depend on characteristics of the benthic community present. Species-specific behavior such as life habit, burrow residence time and irrigation activity, as well as general factors such as the number, size, and spacing of individuals are important in determining biogeochemical microenvironment properties, and thus pH.

The production of CO_2 during the aerobic decomposition of organic matter and the reoxidation of anaerobic metabolites such as NH_4^+, HS^-, and Fe^{2+} sustain relatively acid conditions in sediments and high concentration gradients of $[H^+]$ near the sediment–water interface (Cai and Reimers, 1993; Van Cappellan and Wang, 1996; Cai et al., 2000; Table 1). Formation of NO_3^-, MnOOH, $Fe(OH)_3$, and SO_4^{2-}, with associated release of H^+, and the reduction of O_2 and NO_3^- in the vicinity of the oxic–anoxic redoxcline are primarily responsible for the distinct pH minima often observed near the sediment–water interface and within burrow walls (Table 1). Chemosynthetic bacteria mediate many of these reactions, and elevated bacterial activity is commonly associated with the sedimentary redoxcline region (Yingst and Rhoads, 1980). On the other hand, the anaerobic decomposition of organic matter by oxidants such as MnO_2 or $Fe(OH)_3$ in sediment results in pH increases (Van Cappellan and Wang, 1996; Luther et al., 1999; Cai et al., 2002; Table 1). The pH distribution is an overall balance between these zonally dominant biogeochemical reactions and diffusion processes. In vertically stratified sediments, the pH distribution is controlled by acid production and consumption rates, and one-dimensional vertical transport (Fig. 2A). For sediment containing abundant reduced compounds and intense reoxidation zones, the high concentration of H^+ produces a steep pH gradient just below the water-sediment boundary and relatively low pH values extend well below the pH minimum zone (Fig. 5A). In contrast, the pH at depth is relatively high in less reactive deposits. For example, the pH drop below the overlying water-sediment boundary is about 1.2 pH units over 0.5 cm depth in Flax Pond sediment (Fig. 5A), but is 0.8 pH units over the same depth in central Long Island Sound muds (Fig. 2). The average pH value below the

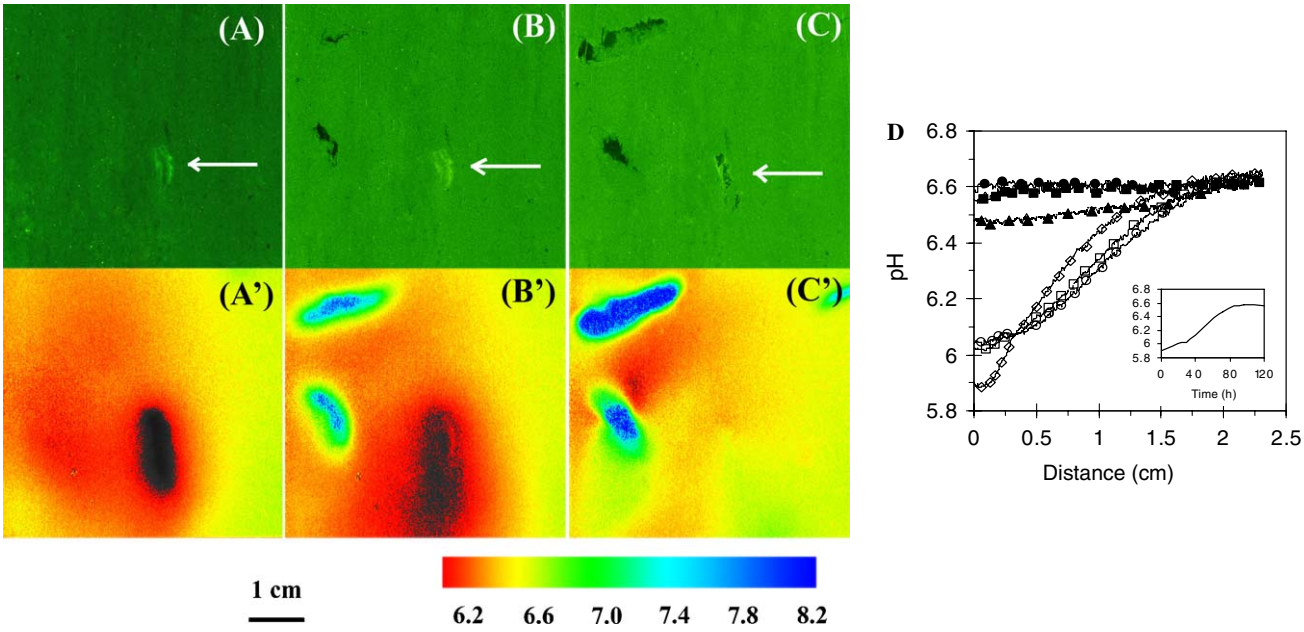

Fig. 10. Dynamic changes of pH around degrading worm tissue in Flax Pond sediment (October 2003). (A–C) Are visible images of the physical structure on day 1, 2, and 5, respectively. The white arrows indicate the site of the decaying biomass. Two new burrow sections appear on the lefthand side of the image plane. (A′), (B′), and (C′) are the corresponding two-dimensional pH patterns respectively, demonstrating pH <6.2 at the center of the decaying mass. (D) The pH diffusion profiles and dynamics in the sandy sediment around the acid spot. Measurements were made at 0 (open square), 24 (open diamond), 30 (open circle), 72 (filled triangle), 96 (filled square), and 120 (filled circle) hours. The insert shows the time dependence of pH at the center of the decay site.

Table 1
Example protonic reactions during early diagenesis

Organic matter decomposition (terminal oxidant series)[a]:

$$CH_2O + O_2 \rightarrow CO_2 + H_2O$$

$$5CH_2O + 4NO_3^- \rightarrow CO_2 + 3H_2O + 4HCO_3^- + 2N_2$$

$$CH_2O + 2MnO_2 + 3CO_2 + H_2O \rightarrow 4HCO_3^- + 2Mn^{2+}$$

$$CH_2O + 4Fe(OH)_3 + 7CO_2 \rightarrow 8HCO_3^- + H_2O + 4Fe^{2+}$$

$$2CH_2O + SO_4^{2-} \rightarrow 2HCO_3^- + H_2S$$

$$2CH_2O \rightarrow CO_2 + CH_4$$

Fermentation (generalized)

$$12CH_2O \rightarrow CH_3CHOHCOOH + 3CH_3COOH + CH_3CH_2OH + CO_2$$

Acid/base equilibria

$$CO_2 + H_2O \leftrightarrow HCO_3^- + H^+$$

$$NH_3 + H^+ \leftrightarrow NH_4^+$$

$$H_3PO_4 \leftrightarrow HPO_4^{2-} + 2H^+$$

$$H_2S \leftrightarrow HS^- + H^+$$

Metabolite / mineral reoxidation:

$$NH_4^+ + 2O_2 \rightarrow NO_3^- + H_2O + 2H^+$$

$$Mn^{2+} + \tfrac{1}{2}O_2 + H_2O \rightarrow MnO_2 + 2H^+$$

$$Fe^{2+} + \tfrac{1}{4}O_2 + \tfrac{5}{2}H_2O \rightarrow Fe(OH)_3 + 2H^+$$

$$Mn^{2+} + \tfrac{2}{5}NO_3^- + \tfrac{4}{5}H_2O \rightarrow MnO_2 + \tfrac{1}{5}N_2 + \tfrac{8}{5}H^+$$

$$Fe^{2+} + \tfrac{1}{5}NO_3^- + \tfrac{12}{5}H_2O \rightarrow Fe(OH)_3 + \tfrac{1}{10}N_2 + \tfrac{9}{5}H^+$$

$$FeS_2 + \tfrac{15}{4}O_2 + \tfrac{14}{4}H_2O \rightarrow Fe(OH)_3 + 2SO_4^{2-} + 4H^+$$

$$FeS_2 + 3NO_3^- + 2H_2O \rightarrow Fe(OH)_3 + 2SO_4^{2-} + \tfrac{3}{2}N_2 + H^+$$

Mineral precipitation / dissolution:

$$2Fe(OH)_3 + 2HS^- + 4H^+ \rightarrow FeS_2 + Fe^{2+} + 6H_2O$$

$$CaCO_3 + H^+ \leftrightarrow Ca^{2+} + HCO_3^-$$

[a] Stoichiometric NH_3 and H_3PO_4 release implicit.

pH minimum zone is about 6.6 in the Flax Pond sediment, but it is 7.2–7.3 in the sediment from central Long Island Sound.

The time course of $[H^+]$ concentration patterns and the establishment of radial zones of acidification and neutralization around new *Nereis* burrows show that the initial acid–base response to burrow formation is dominated by diffusive loss of accumulated pore water $[H^+]$ into the newly formed alkaline cavity (Figs. 4–7). A distinct zone of acid production begins to form within burrow walls soon after exposure to oxygenated seawater. At least in some cases, the net $[H^+]$ production rate, and the corresponding development of inner and outer radial zones of neutralization, increases only slightly after a relatively prolonged period of ~1 week, and then begins to increase substantially (Fig. 7). When an initial period of slowly increasing acid production in the burrow wall is followed by a period of rapid increase (Fig. 7D), the time-dependent pattern is suggestive of the progressive establishment of chemosynthetic microbial populations in association with the redoxcline region of the burrow wall. In other cases, low pH regions rapidly form around transient burrows and then dissipate within 1–2 days (Fig. 4). It seems likely that in intensely burrowed or populated sediments, such as a well burrowed laboratory microcosm, bacterial populations may be poised to respond to burrow formation and irrigation events, enhancing the formation rate of low pH regions within newly generated burrow walls (Fig. 4). Burrow production rates vary inversely with population abundance in a related nereid species and are of the order 1–10 cm $worm^{-1}\ d^{-1}$, giving a sense of the dynamic nature of biogeochemical microenvironmental formation (Miron et al., 1991).

Burrow spacing, the depth at which burrows form, and irrigation frequency must also play strong roles in determining the exact time dependence of acidification zone ingrowth and duration. When dense networks of burrows are present, as on the left side of the *Nereis* burrow in Fig. 5 (Fig. 8), diffusion scales are small and the quantity of sediment between burrows is insufficient to sustain strong $[H^+]$ concentration gradients. Thus, in the extreme burrow density case, sediment takes on a composition close to overlying water. If sediment lacks sufficient reactive reductant (organic matter) or if burrows are not irrigated frequently enough to maintain a well established, high-flux redoxcline, then the formation of an acid production zone around burrow structures may also be minimized.

It is not possible with measurements of pH alone to assign acid production to specific reactions in the burrow walls, however, the calculated acid production rates, up to ~100 nmol cm^{-3} pore water d^{-1}, are in the range expected for reactive, metal-rich marine sediments underlying oxygenated waters, based on both measured respiration rates and diagenetic models (Canfield et al., 1993; Van Cappellan and Wang, 1996; Aller et al., 2004; Middelburg et al., 2004). As shown by the spatial patterns of flux and reaction rates, the neutralization of the $[H^+]$ that is produced occurs largely within the sediment around the burrow and the inner burrow wall rather than in the burrow water (Fig. 7C). Thus, in addition to titration of H^+ by diffusion of HCO_3^- and CO_3^{2-} from adjacent seawater and porewater reservoirs, mineral surface exchange, reduction, and dissolution reactions are likely to be involved in $[H^+]$ consumption (e.g., Farr et al., 1970; Brassard et al., 1996; Table 1).

Low pH domains can form in sediments by processes other than oxic irrigation of burrows and establishment of radial redoxclines. The subsurface entombment and anaerobic decay of reactive biomass clearly results in transient, local acidification associated with the decomposing mass. Acid regions dissipate over periods of several days

when macrofaunal size material is involved (Fig. 10). pH patterns associated with abandoned, infilled burrows are potentially particularly important because of the constant movement and relocation of animals within deposits, and the generation of biogenic fabric. At least in the case of *N. incisa* burrows, infilled structures become low pH sites (Fig. 9), which because there is no O_2 supply from irrigation, indicates locally enhanced anaerobic decomposition rather than processes directly related to redoxcline development. The relict burrow walls and infill retain a light color, indicating the presence of reactive Fe, Mn-oxides and at least partial supply of fill material from the upper surface sediment. It is also likely that mucus secretions are elevated in the vicinity of burrows. These two factors, reactive reductant substrates (mucus, surface sediment) and energetically favorable secondary oxidants NO_3^-, metal oxides), are presumably responsible for locally enhanced decomposition. The time scale of dissipation of these low pH domains ranges from a few days to a week, consistent with that for the decomposition of a reactive organic substrate. A related polychaete species, *Nepthys caeca*, forms burrow lengths of ~12 to 27 cm $worm^{-1}$ d^{-1} depending on temperature (4–10.5 °C), illustrating the potential for relict burrow formation (Caron et al., 1996). These observations demonstrate that the movement of fauna through sediments, and their burrow construction activities, create a complex meshwork of both actively forming (burrow wall redoxcline) and relict pH distributions (filled reactive pockets) which dissipate slowly as fauna move on.

Because pH reflects metabolic acid production and consumption, these complex pH patterns are measures of the distribution of microbial activity and coupling between biogeochemical reaction zones. The important role of bioturbation activity in promoting biogeochemical diversity in benthic communities and its potential impact on elemental cycles are immediately obvious from these patterns (Aller, 1982, 2001; Kristensen, 1988; Solan et al., 2004). Use of mean pH values in consideration of mineral saturation states, adsorption equilibria, or solute speciation can clearly be a misleading indicator of reaction conditions, particularly for the rates nonlinear kinetic processes. Reactions such as hydrolysis and dissolution reactions with high order kinetic dependences on $[H^+]$ can be expected to show extreme spatial variation with little semblance to the mean pH distribution (Aller, 2001; Meile and Tuncay, 2006). The observed variation of pH around burrows is a direct illustration of the wide range of reactions possible at all depths within bioturbated deposits. The close juxtaposition of acidic and alkaline conditions, for example, may support carbonate dissolution and precipitation within the same vertical interval (Fig. 7).

5. Conclusions

The planar optode sensor reveals a wide range of pH distributions and corresponding biogeochemical reaction dynamics in surface marine sediments. In the absence of distinct burrow structures, two-dimensional distributions can show largely planar symmetry below the sediment water interface and can be approximated by one-dimensional vertical profiles. In contrast, actively irrigated and relict biogenic structures can be sites of relatively low pH, resulting in complex, time-dependent spatial patterns of pH in the bioturbated zone. The scaling of pH distributions is determined by faunal size, abundance, irrigation, burrow construction, and burrowing activity. Microenvironmental acidification is associated with redoxcline regions, suggestive of chemoautotrophic activity around well irrigated burrows. Low pH also occurs in relict structures which retain locally elevated levels of reactive substrates. Acid production zones near the redoxcline grow in around burrows over timescales of ~1 to 7 days. Most acid is titrated within the inner burrow wall and surrounding sediment, with only a small proportion released directly into seawater. Two-dimensional resolution of concentration patterns is essential for conceptualizing and modeling heterogeneous biogeochemical reactions, microbial metabolism, and solute transport in bioturbated deposits. The distributions and relationships revealed by this and future solute specific fluorosensors will significantly improve quantitative understanding of biogeochemical processes in the surficial zone of marine sediments and, with minor modification, soils.

Acknowledgments

We thank R. N. Glud, David J. Burdige, and two anonymous reviewers for critical scientific and editorial comments. This work was supported by the Camille and Henry Dreyfus Foundation, the Petroleum Research Fund, and by U.S. National Science Foundation Grants OCE0117062 and OCE0526410.

Associate editor: David J. Burdige

References

Aller, R.C., 1980. Diagenetic processes near the sediment–water interface of Long Island Sound, I: decomposition and nutrient element geochemistry (S,N,P). In: Saltzman, B. (Ed.), *Physics and Chemistry of Estuaries: Studies in Long Island Sound. Adv. in Geophy.*, 22. Academic Press, NY, pp. 235–348.

Aller, R.C., 1982. The effects of macrobenthos on chemical properties of marine sediment and overlying water. In: McCall, P.L., Tevesz, M.J.S. (Eds.), *Animal–Sediment Relation*. Plenum, New York, pp. 53–102.

Aller, R.C., 1994. The sedimentary Mn cycle in Long Island Sound: its role as intermediate oxidant and the influence of bioturbation, O_2, and C_{org} flux on diagenetic reaction balance. *J. Mar. Res.* **52**, 259–295.

Aller, R.C., 2001. Transport and reactions in the bioirrigated zone. In: Boudreau, B.P., Jørgensen, B.B. (Eds.), *The Benthic Boundary Layer*. Oxford University Press, Oxford, pp. 269–301.

Aller, R.C., Aller, J.Y., 1992. Meiofauna and solute transport in marine muds. *Limnol. Oceanogr.* **37**, 1018–1033.

Aller, R.C., Heilbrun, C., Panzeca, C., Zhu, Z.B., Baltzer, F., 2004. Coupling between sedimentary dynamics, early diagenetic processes, and biogeochemical cycling in the Amazon-Guianas mobile mud belt: coastal French Guiana. *Mar. Geol.* **208**, 331–360.

Aller, R.C. and Zhu, Q.Z. (2005) Optical pH sensor. *US Patent*. Application number: US10/973,663.

Boudreau, B.P., 1997. A one-dimensional model for bed boundary layer particle exchange. *J. Mar. Syst.* **11**, 279–303.

Boudreau, B.P., Canfield, D.E., 1993. A comparison of closed-system and open-system models for porewater pH and calcite-saturation state. *Geochim. Cosmochim. Acta* **57**, 317–334.

Boudreau, B.P., Meysman, F.J.R., Middelburg, J.J., 2004. Multicomponent ionic diffusion in porewaters: Coulombic effects revisited. *Earth Planet. Sci. Lett.* **222**, 653–666.

Brassard, P., Macedo, E., Fish, S., 1996. Diffusion and binding of protons in sediments. *Environ. Sci. Technol.* **30**, 3216–3222.

Cai, W.-J., Reimers, C.E., 1993. The development of pH and pCO_2 microelectrodes for studying the carbonate chemistry of pore waters near the sediment-water interface. *Limnol. Oceanogr.* **38**, 1762–1773.

Cai, W.-J., Reimers, C.E., Shaw, T., 1995. Microelectrode studies of organic carbon degradation and calcite dissolution at a California continental rise site. *Geochim. Cosmochim. Acta* **59**, 497–511.

Cai, W.-J., Zhao, P., Wang, Y., 2000. pH and pCO_2 microelectrode measurements and the diffusive behavior of carbon dioxide species in coastal marine sediments. *Mar. Chem.* **70**, 133–148.

Cai, W.-J., Zhao, P., Wang, Y., Theberge, S.M., Witter, A., Luther, G.W., 2002. Porewater redox species, pH and pCO_2 in aquatic sediments. In: Taillefert, M., Rozan, T. (Eds.), *Environmental Electrochemistry: Analysis of Trace Element Biogeochemistry*, vol. 811. American Chemical Society Symposium Series; American Chemical Society, Washtington, DC, pp. 188–209, Ch.10.

Canfield, D.E., Jørgensen, B.B., Fossing, H., Glud, R.N., Gundersen, J., Ramsing, N.B., Thamdrup, B., Hansen, J.W., Nielsen, L.P., Hall, R.O.J., 1993. Pathways of organic carbon oxidation in three continental margin sediments. *Mar. Geol.* **113**, 27–40.

Caron, A., Desrosiers, G., Retière, C., Brenot, S., 1996. Occupation des sédiment par le polychète *Nephtys caeca* en conditions contrôlées. *C.R. Acad. Sci. Paris, Sci. de la vie.* **319**, 417–423.

Dickson, A.G., 1993. The measurement of sea water pH. *Mar. Chem.* **44**, 131–142.

Farr, E., Vaidyanathan, L.V., Nye, P.H., 1970. The measurement and mechanism of ion diffusion in soils V. Diffusion of hydrogen ion in soils. *J. Soil Sci.* **21**, 1–14.

Frederiksen, M.S., Glud, R.N., 2006. Oxygen dynamics in the rhizosphere of *Zostera marina*: A two-dimensional planar optode study. *Limnol. Oceanogr.* **51**, 1072–1083.

Glud, R.N., Fenchel, T., 1999. The importance of ciliates for interstitial solute transport in benthic communities. *Mar. Ecol. Prog. Ser.* **186**, 87–93.

Glud, R.N., Ramsing, N.B., Gundersen, J.K., Klimant, I., 1996. Planar optrodes: a new tool for fine scale measurements of two-dimensional O_2 distribution in benthic communities. *Mar. Ecol. Prog. Ser.* **140**, 217–226.

Glud, R.N., Tengberg, A., Kühl, M., Hall, P.O.J., Klimant, I., 2001. An in situ instrument for planar O_2 optode measurements at benthic interfaces. *Limnol. Oceanogr.* **46**, 2073–2080.

Hales, B., Emerson, S., 1997. Calcite dissolution in sediments of the Ceara rise: in situ measurements of pore water O_2, pH and CO_2. *Geochim. Cosmochim. Acta* **61**, 501–514.

Hannides, A.K., Dunn, S.M., Aller, R.C., 2005. Diffusion of organic and inorganic solutes through macrofaunal mucus secretions and tube linings in marine sediments. *J. Mar. Res.* **63**, 957–981.

Hansson, I., 1973. A new set of pH scales and standard buffers for sea water. *Deep-Sea Res.* **20**, 479–491.

Holst, G., Grunwald, B., 2001. Luminescence lifetime imaging with transparent oxygen optodes. *Sensor. Actuat. B Chem.* **74**, 78–90.

Hulth, S., Aller, R.C., Engström, P., Selander, E., 2002. A pH plate fluorosensor (optode) for early diagenetic studies of marine sediments. *Limnol. Oceanogr.* **47**, 212–220.

Kermis, H.R., Kostov, Y., Harms, P., Rao, G., 2002. Dual excitation ratiometric pH sensor for noninvasive bioprocess monitoring: development and application. *Biotechnol. Prog.* **18**, 1047–1053.

King, D.W., Kester, D.R., 1989. Determination of seawater pH from 1.5 to 8.5 using colorimetric indicators. *Mar. Chem.* **26**, 5–20.

Komada, T., Reimers, C.E., Noehme, S.E., 1998. Dissolved inorganic carbon profiles and fluxes determined using pH and pCO_2 microelectrodes. *Limnol. Oceanogr.* **43**, 769–781.

Kristensen, E., 1988. Benthic fauna and biogeochemical processes in marine sediments: microbial activities and flux. In: Blackburn, T.H., Sørensen, J. (Eds.), *Nitrogen Cycling in Coastal Marine Environments*. Wiley, New York, pp. 275–299.

Leiner, M.J.P., Hartmann, P., 1993. Theory and practice in optical pH sensing. *Sensor. Actuat. B* **11**, 281–289.

Luther III, G.W., Reimers, C.E., Nuzzio, D.B., Lovalvo, D., 1999. In situ development of voltammetric, potentiometric and amperometric microelectrodes from a ROV to determine O_2, Mn, Fe, S(-2) and pH in porewaters. *Environ. Sci. Technol.* **33**, 4352–4356.

Marinelli, R.L., Boudreau, B.P., 1996. An experimental and modeling study of pH and related solutes in an irrigated anoxic coastal sediment. *J. Mar. Res.* **54**, 939–966.

Meile, C., Tuncay, K., 2006. Scale dependence of reaction rates in porous media. *Adv. Water Resour.* **29**, 62–71.

Middelburg, J.J., Duarte, C.M., Gattuso, J.P., 2004. Respiration in coastal benthic communities. In: del Giorgio, P.A., leB Williams, P.J. (Eds.), *Respiration in Aquatic Ecosystems*. Oxford University Press, New York, pp. 207–225.

Millero, F.J., 1986. The pH of estuarine waters. *Limnol. Oceanogr.* **31**, 839–847.

Miron, G., Desrosiers, G., Retière, C., Lambert, R., 1991. Évolution spatio-temporelle du réseau de galeries chez le polychète *Nereis virens* (Sars) en relation avec la densité. *Can. J. Zool.* **69**, 39–42.

Montlucon, D.B., Lee, C., 2001. Factors affecting lysine sorption in a coastal sediment. *Org. Geochem.* **32**, 933–942.

Precht, E., Franke, U., Polerecky, L., Huettel, M., 2004. Oxygen dynamics in permeable sediments with wave-driven pore water exchange. *Limnol. Oceanogr.* **49**, 693–705.

Reimers, C.E., Ruttenberg, K.C., Canfield, D.E., Christiansen, M.B., Martin, J.B., 1996. Porewater pH and authigenic phases formed in the uppermost sediments of the Santa Barbara Basin. *Geochim. Cosmochim. Acta* **60**, 4037–4057.

Solan, M., Cardinale, B.J., Downing, A.L., Engelhardt, K.A.M., Ruesink, J.L., Srivastava, D.S., 2004. Extinction and ecosystem function in the marine benthos. *Science* **306**, 1177–1180.

Stahl, H., Glud, A., Schröder, C., Klimant, I., Tengberg, A. and Glud, R.N., 2006. Time-resolved pH imaging in marine sediments with a luminescent planar optode. Limnol. Oceanogr. Methods (in press).

Strömberg, N., Hulth, S., 2001. Ammonium selective fluorosensor based on the principles of coextraction. *Anal. Chim. Acta* **443**, 215–225.

Swider, K.T., Mackin, J.E., 1989. Transformations of sulfur compounds in marsh-flat sediments. *Geochim. Cosmochim. Acta* **53**, 2311–2323.

Van Cappellan, P., Wang, Y., 1996. Cycling of iron and manganese in surface sediments: a general theory for the coupled transport and reaction of carbon, oxygen, nitrogen, sulfur, iron, and manganese. *Am. J. Sci.* **296**, 197–243.

Wenzhöfer, F., Glud, R.N., 2004. Small-scale spatial and temporal variability in coastal benthic O_2 dynamics: Effects of fauna activity. *Limnol. Oceanogr.* **49**, 1471–1481.

Wolfbeis, O.S., Offenbacher, H., 1986. Fluorescence sensor for monitoring ionic strength and physiological pH values. *Sensor. Actuat.* **9**, 85–91.

Yingst, J.Y., Rhoads, D.C., 1980. The role of bioturbation in the enhancement of bacterial growth rates in marine sediments. In: Tenore, K.R., Coull, B.C. (Eds.), *Marine Benthic Dynamics*. University of South Carolina Press, Columbia, SC, pp. 407–421.

Zhu, Q.Z., Aller, R.C., Fan, Y., 2005. High-performance planar pH fluorosensor for two-dimensional pH measurements in marine sediment and water. *Environ. Sci. Technol.* **39**, 8906–8911.

Zhu, Q.Z., Aller, R.C., Fan, Y., 2006. A new ratiometric, planar fluorosensor for measuring high resolution, two-dimensional pCO_2 distributions in marine sediments. *Mar. Chem.* **101**, 40–53.